AGU100 ADVANCING EARTH AND SPACE SCIENCE

JGR

Journal of Geophysical Research: Oceans

RESEARCH ARTICLE

10.1029/2018JC014248

Satellite Observations of Enhanced Chlorophyll Variability in the Southern California Bight

Thomas Kilpatrick[1], **Shang-Ping Xie**[1], **Arthur J. Miller**[1], **and Niklas Schneider**[2]

[1]Scripps Institution of Oceanography, University of California, San Diego, La Jolla, CA, USA, [2]International Pacific Research Center and Department of Oceanography, University of Hawaii at Manoa, Honolulu, HI, USA

Key Points:
- Satellite observations reveal a "tongue" of elevated chlorophyll that extends into the Southern California Bight from Point Conception
- A local chlorophyll maximum and upwelling cell in the tongue are apparently due to a combination of bathymetric and orographic influences
- The spatial patterns of sea surface temperature influence on chlorophyll variability in the bight vary greatly with time scale

Supporting Information:
- Supporting Information S1

Correspondence to:
T. Kilpatrick,
tkilpatrick@ucsd.edu

Citation:
Kilpatrick, T., Xie, S.-P., Miller, A. J., & Schneider, N. (2018). Satellite observations of enhanced chlorophyll variability in the Southern California Bight. *Journal of Geophysical Research: Oceans*, *123*, 7550–7563. https://doi.org/10.1029/2018JC014248

Received 6 JUN 2018
Accepted 20 SEP 2018
Accepted article online 27 SEP 2018
Published online 29 OCT 2018

Abstract Satellite observations from the Moderate Resolution Imaging Spectroradiometer and Sea-viewing Wide Field-of-view Sensor reveal a "tongue" of elevated near-surface chlorophyll that extends into the Southern California Bight from Point Conception. A local chlorophyll maximum at the western edge of the bight, near the Santa Rosa Ridge, indicates that the chlorophyll is not solely due to advection from Point Conception but is enhanced by local upwelling. Chlorophyll in the bight peaks in May and June, in phase with the seasonal cycle of wind stress curl. The spatial structure and seasonal variability suggest that the local chlorophyll maximum is due to a combination of bathymetric influence from the Santa Rosa Ridge and orographic influence from the coastline bend at Point Conception, which causes sharp wind stress curl in the bight. High-resolution glider observations show thermocline doming in May–June, in support of the local upwelling effect. Despite the evidence for local wind stress curl-forced upwelling in the bight, we cannot rule out alternative mechanisms for the local chlorophyll maximum, such as iron supply from the ridge. Covariability between chlorophyll, surface wind stress, and sea surface temperature (SST) indicates that nonseasonal chlorophyll variability in the bight is closely related to SST, but the spatial patterns of SST influence vary by time scale: Subannual chlorophyll variability is linked to local wind-forced upwelling, while interannual chlorophyll variability is linked to large-scale SST variations over the northeast Pacific. This suggests a greater role for nonlocal processes in the bight's low-frequency chlorophyll variability.

Plain Language Summary Satellite observations of ocean color reveal a "tongue" of enhanced chlorophyll in the Southern California Bight, indicating that this is a region of high biological productivity. The satellite observations and local observations from automated gliders suggest that the enhanced chlorophyll in the bight is due to local upwelling, rather than chlorophyll being simply carried downstream from Point Conception. The seasonal cycle of chlorophyll is in phase with the local wind stress forcing, which peaks in May and June. In contrast to the seasonal variability, the substantial year-to-year chlorophyll variations are controlled by large-scale climate variability over the northeast Pacific, that is, El Niño and marine heat wave events.

1. Introduction

The Southern California Bight is distinct from other regions of the California Current System (CCS), characterized by a wide continental margin and orographic influence from the coastline bend at Point Conception (Hickey, 1998). The coastline bend shields the inner part of the bight from the strong alongshore wind stress that prevails in the immediate regions to the north and south, resulting in strong wind stress curl in the bight (Bakun & Nelson, 1991; Koracin et al., 2004; Seo et al., 2012).

The seasonal cycle of wind stress curl in the bight peaks in May and June, helping to force a cyclonic surface circulation in the southern CCS, with peak poleward flow in the bight during summer (Bray et al., 1999; Di Lorenzo, 2003; Lynn & Simpson, 1987; Todd et al., 2011). The poleward flow advects warm and salty water into the bight, creating a sea surface temperature (SST) front between the coast and cold upwelled water further offshore.

Interannual variability in the CCS region is due to a combination of remote and local forcings. The El Niño–Southern Oscillation (ENSO) influences the CCS via coastally trapped waves (Chelton & Davis, 1982; Dottori & Clarke, 2009; Enfield & Allen, 1980) and via an atmospheric teleconnection that typically weakens upwelling winds during El Niño events (Schwing et al., 2002). However, there is considerable variation among

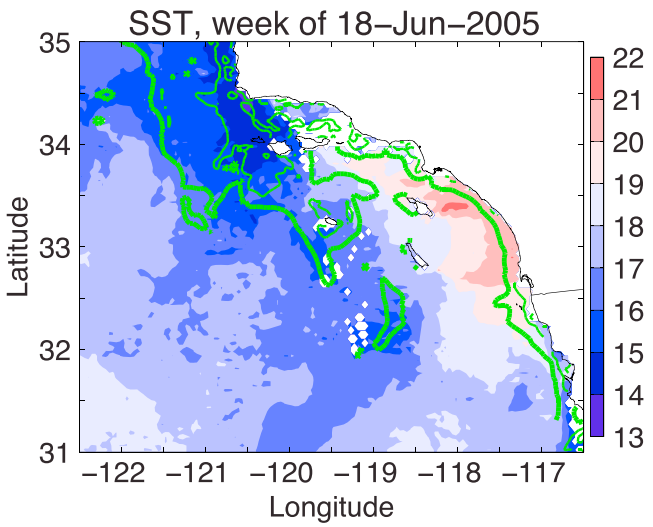

Figure 1. Moderate Resolution Imaging Spectroradiometer SST (shade; °C) and log-transformed chlorophyll (green contours; $\log_{10}$[mg/m^3]) for the 8-day period beginning 18 June 2005. The thick contour marks $\log_{10}$(Chl) = 0; thin contours mark $\log_{10}$(Chl) = 0.5 and 1.0. White dots indicate missing data. Note the tongue of cool SST and high chlorophyll that extends from Point Conception into the bight. SST = sea surface temperature.

CCS responses to individual El Niño and La Niña events (Fiedler & Mantua, 2017; Jacox et al., 2015); for example, wind anomalies were upwelling *favorable* for the 2015–2016 El Niño (Frischknecht et al., 2017; Jacox et al., 2016). Water mass anomalies in the CCS are also generated by anomalous advection (Chelton et al., 1982; Freeland et al., 2003; Schneider et al., 2005), sometimes unrelated to ENSO.

Biological properties of the CCS also exhibit prominent seasonal and interannual variability (Venrick, 2012). Regular observations of physical and biological properties have been made since the late 1940s through the California Cooperative Oceanic Fisheries Investigation (CalCOFI), while satellites such as the Sea-viewing Wide Field-of-view Sensor (SeaWiFS; 1997–2010) and the Moderate Resolution Imaging Spectroradiometer (MODIS; 2002 to present) have measured chlorophyll with near daily sampling since the late 1990s. Although these satellites only measure chlorophyll near the surface (Yoder & Kennelly, 2006), the vast increase in spatial and temporal sampling that satellites provide has enabled the study of how physical and biological properties are linked over a range of scales (McClain, 2009).

Prior to SeaWiFS and MODIS, the coastal zone color scanner (CZCS) observed the highest CCS chlorophyll values within a few hundred kilometers of the coast (Strub et al., 1990; Thomas et al., 1994), where the seasonal cycle peaks during the spring and summer upwelling season. The peak chlorophyll occurs 1–2 months earlier off of Baja California than in the central and northern CCS, due to the earlier onset of upwelling winds in the southern CCS (Legaard & Thomas, 2006).

SeaWiFS observed dramatic negative chlorophyll anomalies in the CCS during the 1997–1998 El Niño event (Kahru & Mitchell, 2000; Legaard & Thomas, 2006). Empirical orthogonal function (EOF) analyses of the longer SeaWiFS and MODIS records have shown that chlorophyll varies in phase over much of the CCS on interannual time scales (Jacox et al., 2016; Thomas et al., 2009, 2012); this regional-scale chlorophyll variability is closely associated with variations in SST and sea level, and presumably nutrient availability.

Here we utilize satellite observations of chlorophyll, SST, sea level, and surface winds to identify an upwelling hot spot in the Southern California Bight. An example of this feature is given in Figure 1, which shows MODIS SST and chlorophyll for the 8-day period beginning 18 June 2005; a prominent "tongue" of cold SST and high

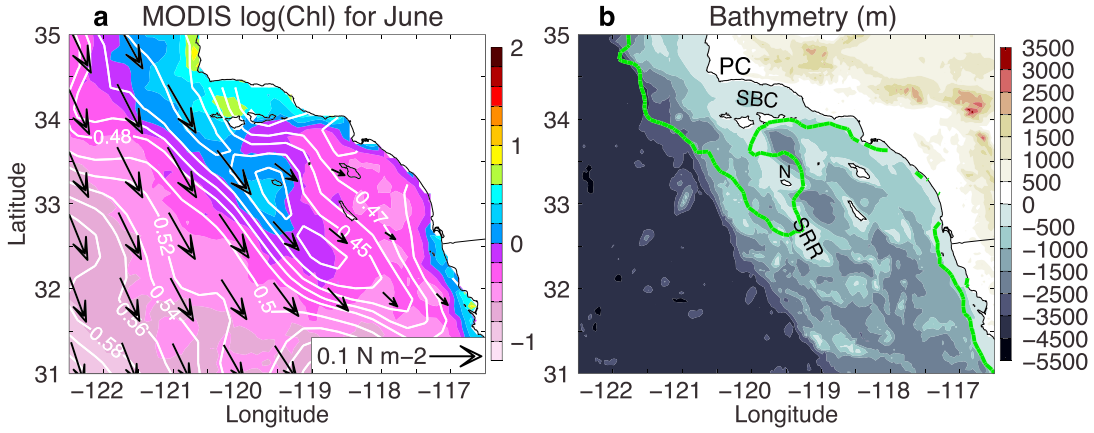

Figure 2. (a) June climatology of MODIS $\log_{10}$(Chl) (color), absolute dynamic topography (contours; cm), and QuikSCAT surface wind stress (N/m^2) for 2002–2009. The coastline bend at PC shields the inner part of the bight from the strong winds that prevail offshore, resulting in wind stress curl. (b) Bathymetry and surface elevation (m), with the June $\log_{10}$(Chl) = 0 contour overlaid in green. Geographical features mentioned in the text are labeled (SRR = Santa Rosa Ridge; PC = Point Conception; SBC = Santa Barbara Channel; N = San Nicolas Island). The chlorophyll tongue is located above the Santa Rosa Ridge. MODIS = Moderate Resolution Imaging Spectroradiometer.

chlorophyll extends from Point Conception into the bight. The tongue feature also appears in chlorophyll climatology, above the Santa Rosa Ridge (Figure 2).

The chlorophyll tongue was identified in early CZCS satellite images: Pelaez and McGowan (1986) described the "latitudinal boundary" that forms the southern edge of the tongue, and Thomas and Strub (1990) considered the seasonal and interannual variability of the same frontal zone, which is sometimes referred to as the Ensenada Front (Chereskin & Niiler, 1994; Landry et al., 2012). Note that Pelaez and McGowan (1986) hypothesized that advection from the high chlorophyll region near Point Conception was responsible for the tongue, but this study emphasizes the role of local wind stress curl-forced upwelling in enhancing the tongue.

We build on Pelaez and McGowan (1986) and Thomas and Strub (1990) by synthesizing observations from multiple satellites over the 1997–2017 period, long enough to consider the seasonal cycle and interannual variability, including two strong El Niño events. Our multisatellite approach is similar to Venegas et al. (2008), who focused on the northern CCS, but we supplement our seasonal analyses with in situ glider observations (section 3.2). Section 2 describes our data and method, section 3 describes seasonal variability, section 4 describes nonseasonal variability, and section 5 closes with a summary.

2. Data and Method

The primary data for this study are chlorophyll and SST observations from the MODIS Aqua satellite, available from 2002. Chlorophyll concentrations in the near-surface ocean are estimated from MODIS observations of ocean color (Hu et al., 2012). We use MODIS Aqua Reprocessing 2018.0 monthly mean chlorophyll data on a ∼9-km grid (NASA Goddard Space Flight Center, O. B. P. G., 2018a) and MODIS monthly mean infrared SST observations on a ∼4-km grid (NASA Goddard Space Flight Center, O. B. P. G., 2014), available from the National Aeronautics and Space Administration Jet Propulsion Laboratory PO.DAAC server. For the 1997–2002 period we use SeaWiFS version 2018 chlorophyll data on a ∼9-km grid (NASA Goddard Space Flight Center, O. B. P. G., 2018b). Chlorophyll data are often nearly log-normally distributed (Campbell, 1995; Gaube et al., 2013), so we log-transform the MODIS and SeaWiFS chlorophyll data prior to computing the seasonal cycle and anomalies.

Orbiting satellite scatterometers provide daily observations of surface wind stress and surface winds over the global oceans by measuring the microwave backscatter from gravity-capillary waves (see Chelton & Freilich, 2005, for an overview of scatterometry). The Quick Scatterometer (QuikSCAT) provided high-quality, 25-km-scale global wind observations from 1999 to 2009. We use the Jet Propulsion Laboratory QuikSCAT version 3.1 vector winds (Fore et al., 2014; SeaPAC, 2013); these are "level 2" data (provided on a grid within the satellite swath) with ∼12.5-km grid spacing. We compute surface stress from the equivalent neutral wind using the modified Large and Pond (1982) neutral-stability drag coefficient and compute spatial derivatives in-swath via line integrals, as advocated by O'Neill et al. (2015). We map the surface winds, stress, and spatial derivatives to a 0.25° grid (Kilpatrick & Xie, 2016). For our analyses of the seasonal cycle in the Southern California Bight (section 3), we focus on the overlap period with MODIS, November 2002 to October 2009.

For our analyses of nonseasonal variability, we utilize surface wind stress from the ERA-Interim reanalysis (Dee et al., 2011), available on a ∼0.7° grid. ERA-Interim covers the combined period of SeaWiFS and MODIS chlorophyll observations (1997–2017), which includes two strong El Niño events. Note that ERA-Interim winds show excellent agreement with QuikSCAT winds for 1999–2009, presumably because QuikSCAT winds are assimilated into the model.

For nonseasonal, regional-scale SST variability we utilize Reynolds et al. (2007) Optimum Interpolation Sea Surface Temperature (OISST) version 2, which combines advanced very high resolution radiometer satellite SST observations with ship and buoy observations, from 1985 to present.

To diagnose surface circulation in the region, we utilize the Copernicus Marine Environment Monitoring Service global ocean gridded level 4 reprocessed sea level anomaly and absolute dynamic topography (formerly distributed by Archiving, Validation, and Interpretation of Satellite Oceanographic (AVISO) data), which is on a 0.25° grid. Observations from the Topex/Poseidon, Jason-1, Jason-2, Jason-3, ERS-1, ERS-2, and Envisat satellite altimeters are merged to form the sea level anomaly and absolute dynamic topography (CMEMS Product User Manual, 2018). The mean dynamic topography used to form the absolute dynamic topography is based on data from the 1993–2012 period (Mulet et al., 2013).

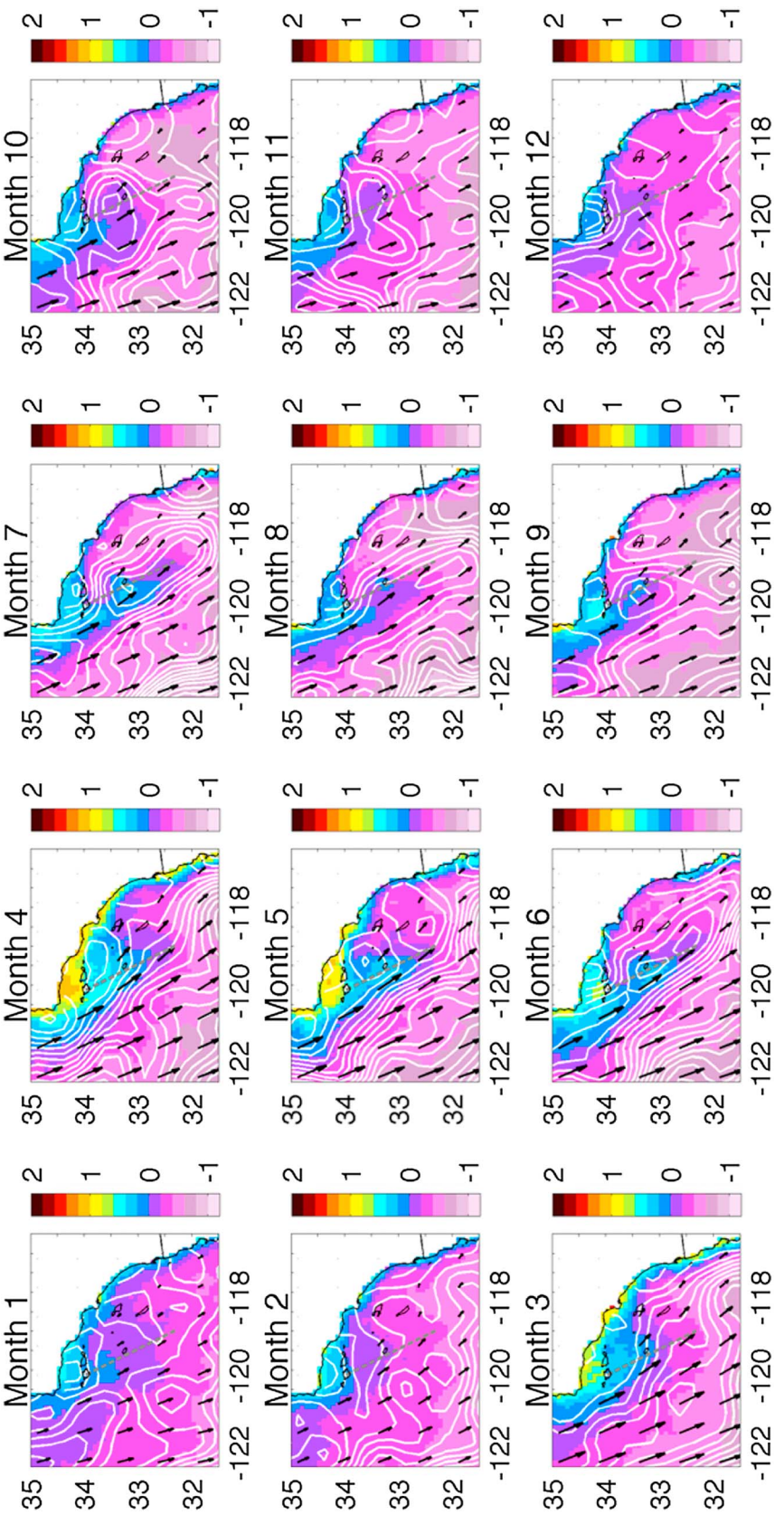

Figure 3. Seasonal cycle of Moderate Resolution Imaging Spectroradiometer $\log_{10}$(Chl) (color) and absolute dynamic topography (white; contour interval [CI] = 1 cm), and Quick Scatterometer surface stress for 2002–2009. The Santa Rosa Ridge location is marked by the gray dashed line. A tongue of elevated chlorophyll near the Santa Rosa Ridge is most prominent in May–July, when wind-forced upwelling is strongest. A cyclonic circulation in the bight, the Southern California Eddy, is strongest in June and July.

We utilize CalCOFI hydrographic and chlorophyll data along Line 90 (Figure S2c in the supporting information) to corroborate the satellite observations. We determine the seasonal cycle of $\log_{10}$(Chl) and potential density via a least squares regression fit to the annual cycle and its first harmonic (see Kim & Cornuelle, 2015).

Here we define the seasonal climatology (section 3) of a given variable as the mean value for each calendar month and nonseasonal variability (section 4) as the departure from that seasonal climatology. For our analyses of nonseasonal variability we apply a low-pass filter to chlorophyll and SST time series, in order to separate low-frequency variations that are associated with large-scale climate variability from high-frequency variations forced by local winds; we use a tanh filter in frequency space, with the filter amplitude reduced to 50% at a frequency of 1 cpy.

3. Seasonal Variability

3.1. Satellite Observations

Near-surface chlorophyll has strong seasonal variability in the CCS, as shown in early CZCS observations (Strub et al., 1990; Thomas et al., 1994; Thomas & Strub, 1990). The seasonal climatology observed by MODIS for the Southern California Bight, 2002–2009, is shown in Figure 3. The largest chlorophyll values in this region are seen in the Santa Barbara Channel in April and May, but of interest here is the tongue of high chlorophyll that extends into the bight along the Santa Rosa Ridge, from roughly April to August. A local chlorophyll maximum appears along the tongue at ~33.1°N, near San Nicolas Island, from May to August. The collocation of the local chlorophyll maximum and the Santa Rosa Ridge is more clearly visible in Figure 2, which shows the June climatology.

Figure 3 also shows the seasonal cycle of absolute dynamic topography and QuikSCAT surface wind stress for 2002–2009. Monthly mean winds are upwelling favorable year-round at this latitude, but the strong seasonal modulation of the winds, with peak wind stress and wind stress curl in the bight in May–June, has a strong influence on the CCS circulation (Marchesiello et al., 2003).

In response to the seasonal cycle of wind stress and wind stress curl, equatorward flow west of the Santa Rosa Ridge strengthens in April, and poleward flow in the bight develops as part of a cyclonic circulation known as the Southern California Eddy (Bray et al., 1999; Lynn & Simpson, 1987; McCreary et al., 1987). The peak poleward flow occurs in June through August, lagging the strongest winds by ~2 months. The region of strongest equatorward flow propagates west from April to August, part of a seasonal Rossby wave (Di Lorenzo, 2003; Todd et al., 2011). By December and January, the offshore equatorward flow is diffuse and the nearshore poleward flow is weak.

Figure 4 shows the seasonal cycle of QuikSCAT wind stress curl (color), with MODIS SST (black) and chlorophyll (green) overlaid. The maximum wind stress curl observed by QuikSCAT exceeds 8×10^{-7} kg·m^{-2}·s^{-2} in May. Sampling in the bight is improved in QuikSCAT version 3.1 due to its reduced land mask (Stiles 2016), but land contamination still obscures the inner part of the bight. Nevertheless, wind stress curl in the bight in QuikSCAT version 3.1 is up to 50% larger than in earlier QuikSCAT versions that suffered more from land contamination (e.g., Risien & Chelton, 2008). (Note that preliminary analyses of QuikSCAT version 4.0 winds indicate further improvements in coverage in the northern part of the bight but show a similar wind distribution near the local chlorophyll maximum [not shown].)

SST contours in Figure 4, though noisy due to sampling variability caused by stratiform clouds (e.g., Clemensha et al., 2016), show that a cold SST tongue develops in phase with the chlorophyll tongue (note that SST contours in the bight are clearer after July, when cloud cover is less persistent). In May through August, "kinks" are visible in the SST contours near 33.3°N, consistent with the cooling effect of wind stress curl-forced upwelling; these cool SST kinks are absent in the NOAA OISST product (not shown). A cross-shore SST gradient develops to the east of the Santa Rosa Ridge and peaks in June, with a maximum change of 2 °C over less than 50 km.

Figure 5a is a Hovmöller diagram of the same MODIS $\log_{10}$(Chl) monthly climatology, with QuikSCAT wind stress curl and sea level overlaid, for a zonal section at 33.1°N. The seasonal coevolution of chlorophyll, winds, and SST is more clearly visible than in the previous plots; the chlorophyll maximum over the Santa Rosa Ridge (~119.6°W) is in phase with wind stress curl (black contours), both peaking in May–June. This seasonality appears to be consistent with early SeaWiFS observations (e.g., Kahru & Mitchell, 2001). Note that the chlorophyll maximum remains over the Santa Rosa Ridge, despite the wind stress curl maximum being located at

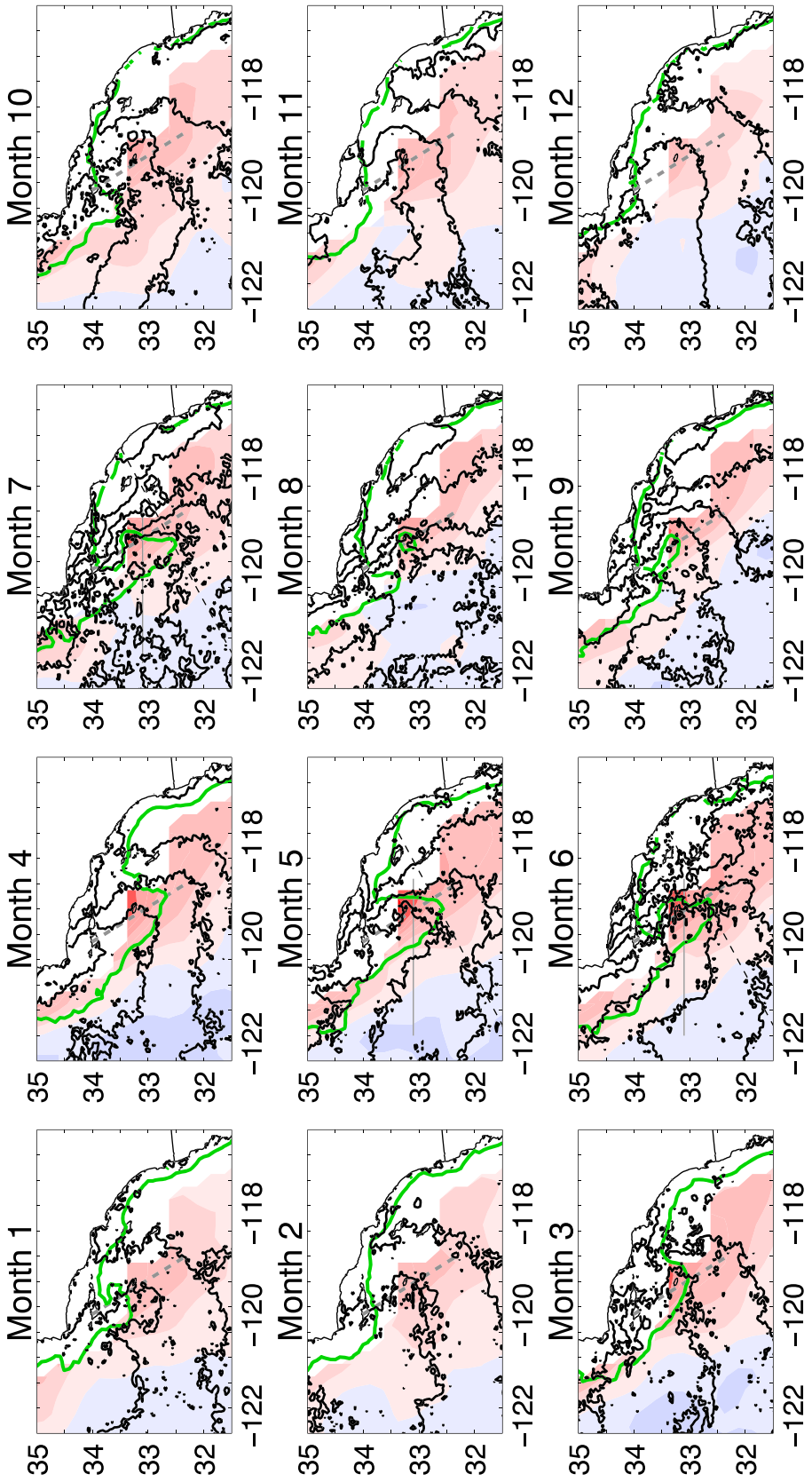

Figure 4. Seasonal cycle of Quick Scatterometer wind stress curl (shade; red is positive and blue is negative, with ±1, ±2, ±4, ±6, and $\pm 8 \times 10^{-7}$ kg·m^{-2}·s^{-2} levels contoured). Moderate Resolution Imaging Spectroradiometer sea surface temperature contours (black; CI= 1 °C) and the $\log_{10}$(Chl) = 0 contour (green) are overlaid. The Santa Rosa Ridge location is marked by the gray dashed line. The May–June panels also mark the location of Line 90 (thin black dashed) and the zonal section used for Figure 5 (thin gray line).

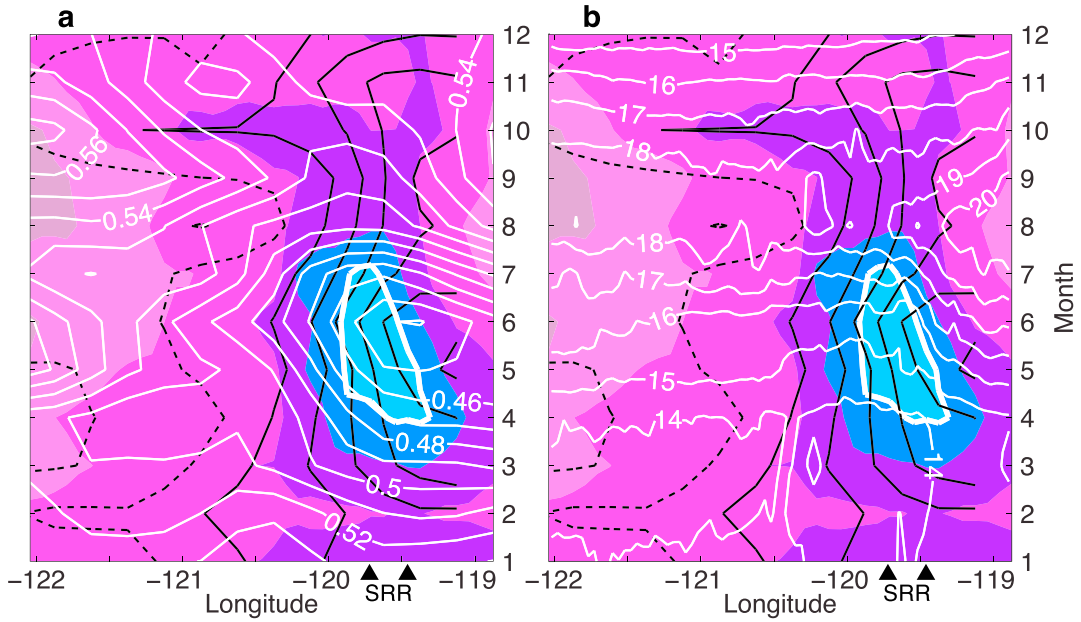

Figure 5. Hovmöller diagram of MODIS $\log_{10}$(Chl) (color) and Quick Scatterometer wind stress curl (black) seasonal cycles at 33.1°N (cf. gray line in May–July panels of Figure 4). Contour intervals for chlorophyll and wind stress curl are the same as Figure 4; the thick white contour marks $\log_{10}$(Chl) = 0.2. Absolute dynamic topography (m) is overlaid in white in (a) and MODIS sea surface temperature (°C) is overlaid in white in (b). Triangles on the abscissa mark the location of the Santa Rosa Ridge. The timing of the chlorophyll maximum in May–June is in phase with the wind stress curl forcing, while the position of the chlorophyll maximum appears to be determined by the ridge. MODIS = Moderate Resolution Imaging Spectroradiometer.

least 50 km to the east (it is not clear whether QuikSCAT resolves the location of the wind stress curl maximum at this latitude, since the land mask obscures the inner part of the bight).

The sea level contours (white) show the spin-up of the Southern California Eddy in response to the wind stress, with equatorward flow to the west of the ridge. Because the largest chlorophyll values in this region occur upstream near Point Conception (Figure 2a), our null hypothesis to explain the May–June chlorophyll maximum in the bight might be advection of chlorophyll from Point Conception (e.g.,Pelaez & McGowan, 1986). However, as shown in Figures 3 and 4, a local chlorophyll *maximum* occurs in the bight, which contradicts this advection hypothesis. Figure 5 also indicates that the location of the chlorophyll maximum at 33.1°N remains over the Santa Rosa Ridge, while the strongest equatorward currents drift west from June to August due to the seasonal Rossby wave (Di Lorenzo, 2003; Todd et al., 2011).

We overlay the MODIS high-resolution infrared daytime SST contours on the chlorophyll Hovmöller diagram in Figure 5b. The SST minimum along this zonal section is located above or slightly to the west of the chlorophyll maximum; SST increases sharply to the east of the Santa Rosa Ridge. We note that the SST gradient east of the ridge is poorly represented in the OISST product (Figure S1 in the supporting information), which smooths the SST gradient across the chlorophyll maximum.

3.2. Glider Observations Along Line 90

Satellite observations of chlorophyll, winds, sea level, and SST give varying perspectives on the surface ocean but cannot reveal the vertical structure of the seasonal upwelling and chlorophyll variability in the bight. Glider data have been collected nearly continuously in this region since 2007 (Rudnick et al., 2017) along Line 90, which intersects the southern part of the chlorophyll tongue (Figure 4, thin dashed line in May–July panels) during the upwelling season.

Glider sections for May–June show isopycnals doming above the Santa Rosa Ridge (Figure 6a) and an SST minimum located ~50 km to the southwest of the ridge. By contrast, isopycnal doming is muted in November–December (Figure 6b).

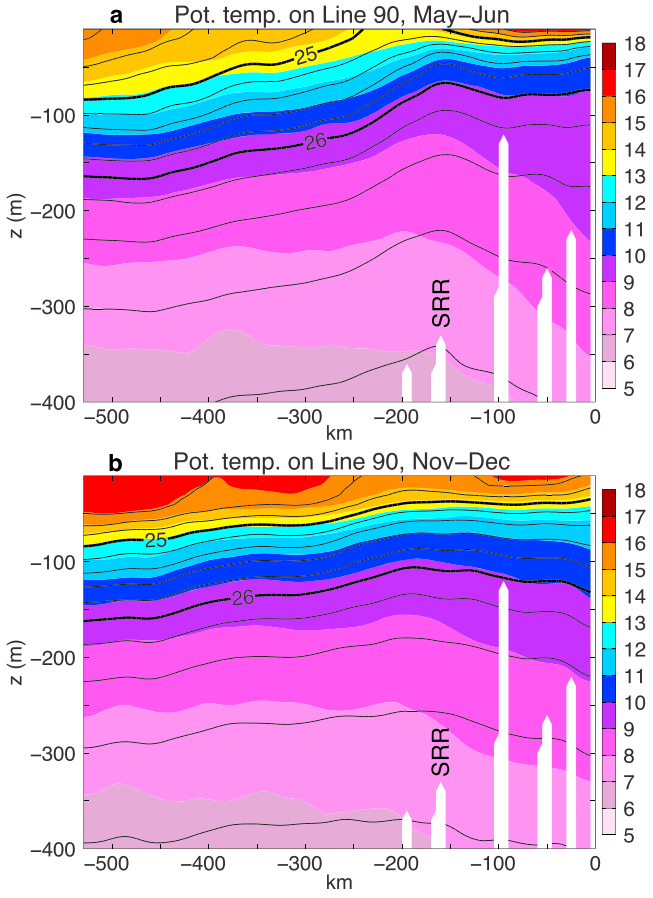

Figure 6. Climatology of potential temperature (color) and potential density (contours) along Line 90 (cf. May–July panels in Figure 4) measured by gliders (Rudnick et al., 2017). The abscissa coordinate is distance from shore. Above the Santa Rosa Ridge (~170 km from shore), doming of isopycnals is apparent in May–June (a) but muted in November–December (b).

The local upwelling cell that is revealed in Figure 6a is concealed in CalCOFI annual mean climatology (e.g., Bograd & Lynn, 2003). It does appear in CalCOFI seasonal mean plots (Figure S2), though the structure is only coarsely resolved due to the ~50-km spacing of CalCOFI stations, thereby illustrating the utility of glider observations, whose horizontal resolution is ~3 km.

Rudnick et al. (2017) noted the temperature minimum above the Santa Rosa Ridge in glider climatology and speculated that it may be due to increased mixing or local upwelling. Johnston and Rudnick (2015) analyzed mixing along Line 90 in some detail and found enhanced mixing above the ridge, with forcing by both the diurnal and semidiurnal internal tides.

The satellite and glider data presented thus far support our hypothesis that wind stress curl-forced upwelling is responsible for the local chlorophyll maximum present in the western part of the bight from May to August. However, other mechanisms may contribute to the location, strength, and timing of the local chlorophyll maximum.

One such process is iron supply from the Santa Rosa Ridge. Recent studies have shown some evidence of iron limitation in this region (King & Barbeau, 2007, 2011), so it is plausible that iron from the ridge could be mixed through the water column and contribute to the annual mean chlorophyll distribution. Observations of vertical mixing along Line 90 show little seasonal variability (Figure 9 in Johnston & Rudnick, 2015), however, so it seems unlikely that iron supply by the ridge is responsible for the seasonally varying chlorophyll tongue shown in Figures 3 and 5. Nevertheless, without more comprehensive observations of iron and species composition in the chlorophyll tongue, we cannot rule out the iron supply hypothesis.

4. Nonseasonal Variability

4.1. Covariability of Chlorophyll and SST

Here we analyze nonseasonal chlorophyll variability in the Southern California Bight for 2002–2017. The standard deviation of MODIS $\log_{10}$(Chl) anomalies (Figure 7) resembles the seasonal chlorophyll maps for spring and summer (cf. Figure 3), with the highest values along the coast in the Santa Barbara Channel, Santa Monica Basin, and San Pedro Basin and in a tongue that extends into the bight.

To represent chlorophyll variability in the bight, we area-average the log-transformed MODIS chlorophyll over the box shown in Figure 7. The time series of area-averaged MODIS chlorophyll and SST are closely related for 2002–2017 (Figure 8a) with a correlation of −0.64; that is, high chlorophyll anomalies are associated with cool SST. This correlation satisfies $p < 10^{-15}$ based on a t test with 102 effective degrees of freedom ($N = 186$ reduced to $N_{\text{eff}} = N(1 - r_1 r_2)/(1 + r_1 r_2)$ to account for the lag-1 autocorrelation in chlorophyll [$r_1 = 0.49$] and SST [$r_2 = 0.59$] time series; Bretherton et al., 1999).

Figure 8a indicates that chlorophyll and SST in the bight have substantial interannual variability, shown by the low-pass time series, and month-to-month or subannual variability, shown by the frequent spikes. The low-pass time series are correlated −0.87 and show clear influence from ENSO, with positive chlorophyll anomalies during the 2007–2008 and 2010–2011 La Niña events, and negative chlorophyll anomalies during the 1997–1998 and 2015–2016 strong El Niño events (Figure S5). However, consistent with Fiedler and Mantua (2017), the bight variability cannot be understood solely in terms of ENSO; for example, the moderate El Niño events of 2002–2003 and 2009–2010 do not show appreciable anomalies in SST or chlorophyll, and the negative chlorophyll anomalies in 2014–2015 do not correspond to an El Niño event.

High-pass time series of chlorophyll and SST (Figure 8b) are not as closely related as the low-pass time series, but spikes in chlorophyll are generally concurrent with spikes in SST. The high-pass time series are correlated −0.37 ($p < 10^{-7}$, based on a t test with 168 degrees of freedom).

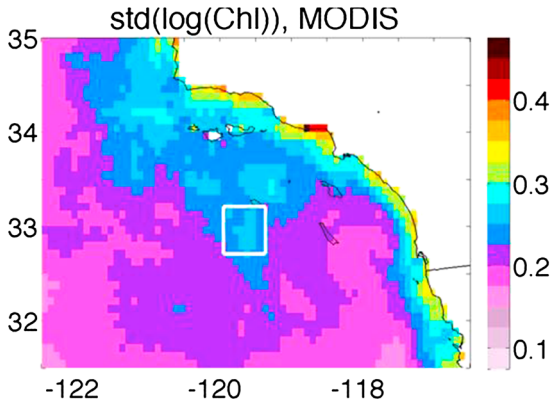

Figure 7. Standard deviation of Moderate Resolution Imaging Spectroradiometer $\log_{10}$(Chl) anomalies, 2002–2017. A tongue-like pattern extends into the bight, similar to climatology. The white box marks the region for our area-averaged chlorophyll signal.

To evaluate the spatial scales of variability associated with the time series in Figure 8, we regress SST over the greater CCS region onto the high-pass and low-pass $\log_{10}$(Chl) time series. The SST regression pattern for the high-pass chlorophyll time series (Figure 9a) shows cool anomalies extending southwest from Point Conception and central California and warm anomalies in a band extending southwest from the Oregon and Washington coasts.

ERA-Interim wind stress regressions onto the high-pass chlorophyll time series are consistent with the SST patterns, with upwelling favorable wind anomalies collocated with the cool SST anomalies off Point Conception and downwelling favorable wind anomalies north of that. The dipole in wind anomalies suggests that the subannual bight chlorophyll variations are associated with meridional shifts in the subtropical high-pressure system that modulates alongshore winds on the North American west coast. The southern CCS wind anomalies in Figure 9a include strong wind stress curl in the Southern California Bight, consistent with Rykaczewski and Checkley (2008). Note that Figure 9a shows the regression pattern constructed using data from May–July only; including data from all months results in a similar regression pattern, albeit with a weaker amplitude (not shown).

The dipole in wind stress anomalies seen in Figure 9a is consistent with two recent studies that show wind anomalies in the southern CCS and northern CCS are negatively correlated on synoptic time scales (Fewings, 2017; Fewings et al., 2016). Fewings (2017) hypothesizes that the wind dipole along the North American west coast would drive opposite-signed upwelling anomalies; this hypothesis appears to be confirmed by Figure 9a.

A very different SST pattern is obtained from regressing unfiltered NOAA OISST anomalies and ERA-Interim wind stress anomalies onto the low-pass $\log_{10}$(Chl) time series (Figure 9b). The SST pattern is same signed, indicating that positive low-pass chlorophyll anomalies in the bight are associated with cool SST over the entire CCS region. ERA-Interim wind stress anomalies regressed onto the low-pass chlorophyll

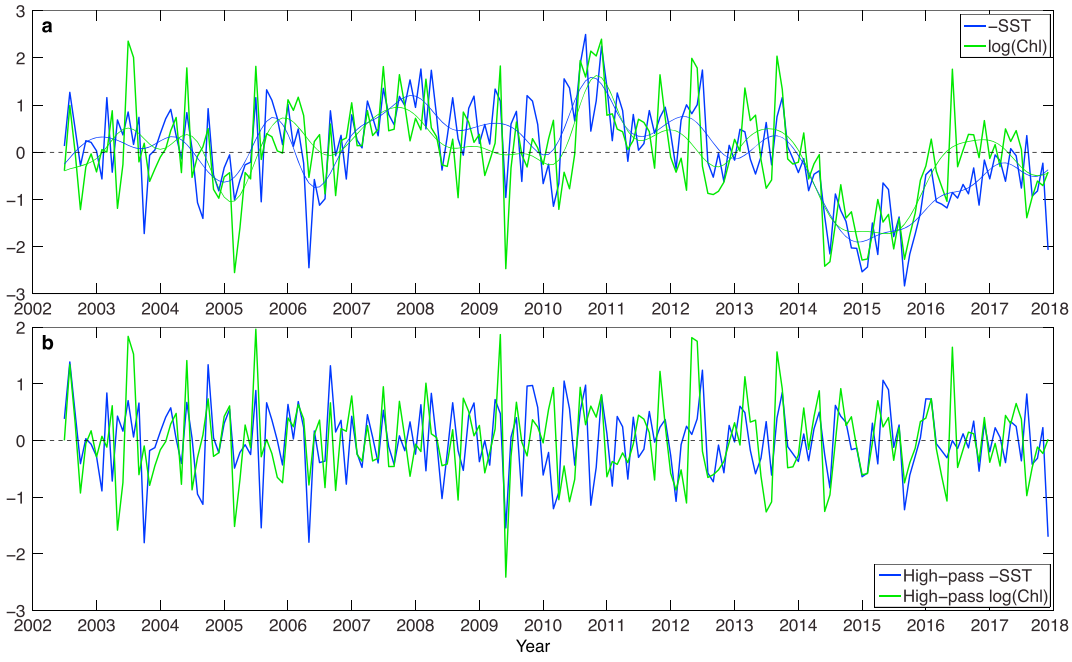

Figure 8. (a) Anomalies of Moderate Resolution Imaging Spectroradiometer $\log_{10}$(Chl) and −SST in the Southern California Bight box, with low-pass anomalies overlaid; both time series are normalized to unit variance. (b) High-pass $\log_{10}$(Chl) and −SST anomalies. Chlorophyll and SST anomalies show agreement across time scales. SST = sea surface temperature.

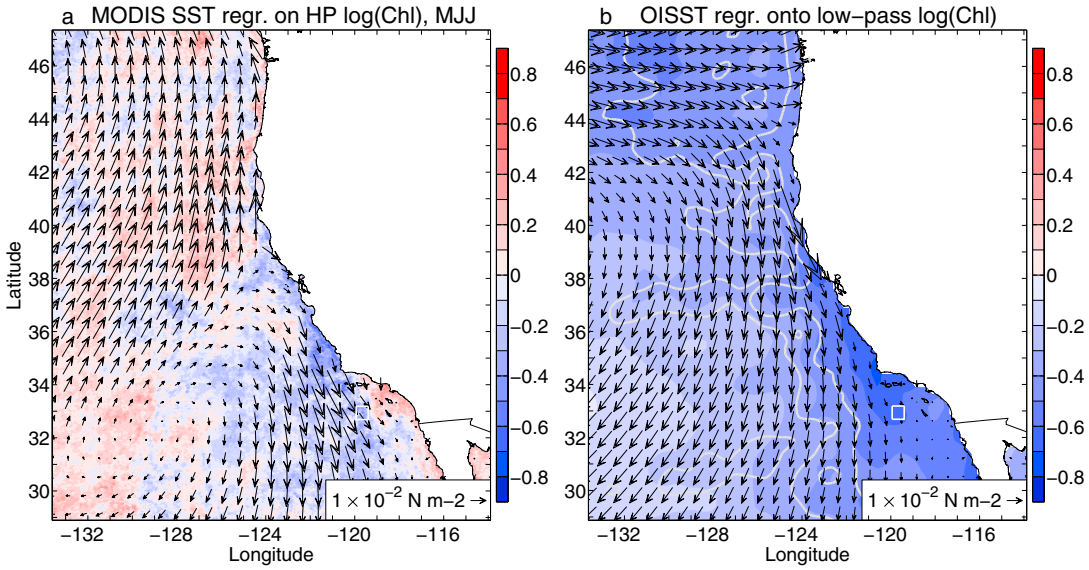

Figure 9. (a) MODIS daytime SST and ERA-Interim surface wind stress regression onto high-pass chlorophyll signal from the bight box for 2002–2017, May–July months only. (b) OISST (color; °C) and ERA-Interim surface wind stress regression onto low-pass chlorophyll signal for 1997–2017. Gray contours in (b) show −1- and −2-cm contours of the sea level anomaly regression onto low-pass chlorophyll. The SST pattern in (b) is same signed over the whole CCS region, reflecting large-scale SST influence on the bight, while the SST pattern in (a) is suggestive of upwelling anomalies off of southern California and downwelling anomalies in the northern California Current System. MODIS = Moderate Resolution Imaging Spectroradiometer; SST = sea surface temperature; OISST = Optimum Interpolation Sea Surface Temperature; MJJ = May–July.

indicate upwelling-favorable wind anomalies with peak amplitude off central California and weak amplitude off Point Conception. Sea level anomalies regressed onto the low-pass chlorophyll indicate low coastal sea level throughout the CCS. Wind anomalies are weak off Baja California and the Southern California Bight, suggesting that SST and sea level anomalies there are remotely forced.

We utilize NOAA OISST instead of MODIS SST for the regression onto low-pass chlorophyll to span the combined observation period of SeaWiFS and MODIS (1997–2017), which includes two strong El Niño events. The MODIS SST regression onto low-pass $\log_{10}$(Chl) for 2002–2017 looks similar to Figure 9b (not shown). The spatial pattern of SeaWiFS chlorophyll variance (Figure S3) looks similar to MODIS chlorophyll variance (cf. Figure 7), and the two sensors show excellent agreement in the bight for the overlap period of 2002–2010 (Figure S4).

Previous analyses of satellite data have shown that chlorophyll, SST, and sea level anomalies show coherent interannual variations along the west coast of North America (e.g., Thomas et al., 2012). However, we are not aware of any prior studies that have demonstrated the distinct SST and wind stress patterns associated with subannual chlorophyll variations in the bight (Figure 9a).

4.2. Interpretation of Distinct SST Patterns

Figure 9 shows distinct SST patterns associated with subannual and interannual chlorophyll variability in the Southern California Bight. The dipole in SST and alongshore wind stress anomalies associated with subannual chlorophyll variability (Figure 9a) suggests that the high-frequency "spikes" seen in the chlorophyll and SST time series (Figure 8) are forced by local wind stress anomalies.

In contrast, the SST pattern associated with low-pass chlorophyll variability in the bight (Figure 9b) shows cool SST over the entire CCS region. The spatial pattern of wind stress anomalies is consistent with upwelling anomalies near Cape Mendocino (~40°N), but not off the Oregon and Washington coast, and not in the southern CCS. Interannual SST variability in the CCS is dominated by large-scale events like ENSO and the marine heat wave ("blob") of 2014–2015 (Bond et al., 2015). The CCS SST anomalies associated with these large-scale events are generated primarily through nonlocal forcing; for example, SST anomalies in the CCS were positive during the 2015–2016 El Niño despite upwelling-favorable wind anomalies (Frischknecht et al., 2017; Jacox et al., 2016).

Table 1
Correlations Between SeaWiFS-MODIS log_{10}(Chl) Monthly Anomalies in the Southern California Bight and Climate Indices, 1997–2017

Chlorophyll	Niño 3.4	Niño 1+2	PDO	NPGO
Unfiltered log_{10}(Chl)	**−0.41** (0.29)	**−0.44** (0.35)	**−0.32** (0.29)	0.19 (0.25)
Low-pass log_{10}(Chl)	**−0.56** (0.39)	**−0.62** (0.47)	**−0.46** (0.39)	0.22 (0.34)

Note. Bold text indicates the magnitude of the correlation exceeds the estimated $p = 0.01$ level, which is in parentheses. PDO = Pacific Decadal Oscillation; NPGO = North Pacific Gyre Oscillation; SeaWiFS = Sea-viewing Wide Field-of-view Sensor; MODIS = Moderate Resolution Imaging Spectroradiometer.

To highlight the nonlocal forcing of interannual SST variability, we perform maximum covariance analysis (MCA) in the Southern California Bight region for 1997–2017. MCA analysis is also known as singular value decomposition of the covariance matrix for two fields (Bretherton et al., 1992) and identifies the spatial patterns that maximize covariance between two fields, analogous to how an EOF analysis identifies the pattern that accounts for the most variance in one field. The dominant pattern of covariability between wind stress and SST does a poor job of explaining the large warming during the 1997–1998 El Niño, the 2014–2015 marine heat wave, and 2015–2016 El Niño (Figure S6).

We hypothesize that the strong relationship between chlorophyll and SST in the bight is due to the close relationship between SST, thermocline depth, and nutrient availability; that is, low-frequency variations in chlorophyll are likely related to low-frequency variations in nutricline depth. The low-frequency thermocline depth variations are largely of nonlocal origin and propagate into the CCS region via coastally trapped waves. The negative coastal sea level anomalies in Figure 9b suggest that anomalous alongshore advection (Chelton et al., 1982; Kilpatrick et al., 2011; Schneider et al., 2005) also contributes to low-frequency nutrient anomalies in the CCS.

Lastly, we summarize correlations between the bight chlorophyll anomaly and the unfiltered Niño 3.4, Niño 1+2, Pacific Decadal Oscillation (Mantua et al., 1997; Schneider & Cornuelle, 2005), and North Pacific Gyre Oscillation (NPGO; Di Lorenzo et al., 2008) indices in Table 1. The $p = 0.01$ levels for these correlations are estimated from the "random phase test" (Ebisuzaki, 1997).

The El Niño and Pacific Decadal Oscillation correlations exceed the $p = 0.01$ level for this time period, which is not surprising since chlorophyll is so closely linked to SST. Note that chlorophyll is correlated more strongly to Niño 1+2 than to Niño 3.4, hinting that El Niño influences chlorophyll in the bight more through coastally trapped waves than through atmospheric teleconnections. The NPGO is correlated at only the $p = 0.08$ and $p = 0.14$ levels to the unfiltered log_{10}(Chl) and low-pass log_{10}(Chl) time series, respectively. The weak correlations to the NPGO are somewhat surprising since Di Lorenzo et al. (2008) showed the NPGO is correlated with low-frequency CCS variability in chlorophyll and nutrients over 1985–2004. Some of this discrepancy may be due to the different time periods, and some due to our use of satellite observations in a relatively small area, whereas Di Lorenzo et al. (2008) considered CalCOFI observations over the larger southern CCS region.

5. Summary

Satellite observations from MODIS reveal a chlorophyll tongue that extends from Point Conception into the Southern California Bight, along a bathymetric feature known as the Santa Rosa Ridge (Figure 2). A local chlorophyll maximum is visible in the bight from May to July (Figure 3), suggesting that the chlorophyll is not simply advected into the bight but is enhanced by local processes in the bight. Chlorophyll in the bight peaks from May to June, in phase with the seasonal cycle of QuikSCAT wind stress curl, suggesting a central role for Ekman pumping. However, the chlorophyll maximum remains above the Santa Rosa Ridge through the upwelling season, while the wind stress curl maximum is ∼50 km to the east (Figure 5), pointing to the joint influence of orographic winds and bathymetry. Glider observations corroborate the local upwelling cell (Figure 6).

We find a negative correlation between chlorophyll and SST anomalies in the bight across time scales (Figure 8). Strong month-to-month or subannual chlorophyll variability is associated with local wind-forced upwelling (Figure 9a). In contrast, low-frequency chlorophyll variability in the bight is associated with SST variability that is coherent over the whole CCS (Figure 9b). Large-scale SST variability associated with ENSO

and the 2014–2015 marine heat wave is primarily forced by nonlocal processes, suggesting a greater role for nonlocal forcing in the bight's low-frequency chlorophyll variability.

The upwelling hot spot we find in the Southern California Bight is reminiscent of orographic wind jets in the lee of Hawaii's Big Island (Chavanne et al., 2002; Xie et al., 2001) and in the Canary Islands (Basterretxea et al., 2002). The coastline bend at Point Conception shields the inner part of the bight from the strong alongshore winds that prevail over other parts of the CCS and results in positive wind stress curl that peaks 100–150 km from shore (Figures 2a and 4). However, the Southern California Bight differs from these other regions in the bathymetric influence of the Santa Rosa Ridge, which appears to anchor the upwelling cell and chlorophyll maximum.

Although the satellite and glider data presented here are consistent with our hypothesis of wind stress curl-forced upwelling causing the local chlorophyll maximum in the bight, we cannot rule out alternative mechanisms such as iron supply from the ridge. Recent studies have shown some evidence of iron limitation in the bight (King & Barbeau, 2007, 2011), so it is plausible that iron supply from the ridge could contribute to the location, strength, and timing of the chlorophyll tongue. However, glider data show little seasonal variability in vertical mixing along Line 90, so we think it is unlikely that iron supply from the ridge causes the seasonally varying chlorophyll tongue, especially in light of the observed relation between chlorophyll and temperature at seasonal (section 3) at nonseasonal (section 4) time scales.

Several studies have emphasized the importance of bathymetry for the bight's surface circulation (Dong et al., 2009, 2012; Hickey, 1992), but the mechanisms that maintain the chlorophyll maximum above the ridge are unknown. The linear Ekman pumping invoked above seems inconsistent with the apparent displacement between the local chlorophyll maximum and the wind stress curl maximum (Figure 5). Numerical experiments would be helpful to determine the relative importance of processes such as Ekman pumping and tidal mixing (e.g., Johnston & Rudnick, 2015). A field experiment could help determine whether elevated chlorophyll in the tongue is due to macronutrient supply, as hypothesized here, or other mechanisms such as iron supply from the ridge; the species composition in the tongue might help determine how much of the chlorophyll is due to advection from Point Conception, and how much is due to local upwelling.

Acknowledgments
MODIS chlorophyll and SST data are processed by the Ocean Biology Processing Group at NASA's Goddard Space Flight Center. SSALTO/DUACS sea level data were downloaded from CMEMS (http://marine.copernicus.eu/, product identifier SEALEVEL_GLO_PHY_L4_REP_OBSERVATIONS_008_047). Spray glider data from the California Underwater Glider Network are available at https://doi.org/10.21238/S8SPRAY7292. CalCOFI chlorophyll and hydrographic data are available at http://www.calcofi.org/ccdata.html. The El Niño and PDO indices are available at https://www.esrl.noaa.gov/psd/gcos_wgsp/Timeseries and the NPGO index is available at http://www.o3d.org/npgo. We thank Drs. Nick Siler, Janet Sprintall, Pete Gaube, Melanie Fewings, Dan Rudnick, and Kathy Barbeau for valuable discussions. S. -P. X., T. K., and N. S. are supported by the NASA Ocean Vector Winds Science Team (NNX14AL83G); A. J. M. is supported by NSF CCE-LTER (OCE-1637632) and NOAA MAPP (NA17OAR4310106).

References

Bakun, A., & Nelson, C. S. (1991). The seasonal cycle of wind-stress curl in subtropical eastern boundary current regions. *Journal of Physical Oceanography*, *21*, 1815–1834.

Basterretxea, G., Barton, E. D., Tett, P., Sangra, P., Navarro-Perez, E., & Aristegui, J. (2002). Eddy and deep chlorophyl maximum response to wind-shear in the lee of Gran Canaria. *Deep-Sea Research Part I*, *49*, 1087–1101. https://doi.org/10.1016/S0967-0637(02)00009-2

Bograd, S. J., & Lynn, R. J. (2003). Long-term variability in the Southern California Current System. *Deep-Sea Research Part II*, *50*, 2355–2370. https://doi.org/10.1016/S0967-0645(03)00131-0

Bond, N. A., Cronin, M. F., Freeland, H., & Mantua, N. (2015). Causes and impacts of the 2014 warm anomaly in the NE Pacific. *Geophysical Research Letters*, *42*, 3414–3420. https://doi.org/10.1002/2015GL063306

Bray, N. A., Keyes, A., & Morawitz, W. M. L. (1999). The California current system in the Southern California Bight and the Santa Barbara Channel. *Journal of Geophysical Research*, *104*, 7695–7714. https://doi.org/10.1029/1998JC900038

Bretherton, C. S., Smith, C., & Wallace, J. M. (1992). An intercomparison of methods for finding coupled patterns in climate data. *Journal of Climate*, *5*, 541–560.

Bretherton, C. S., Widmann, M., Dymnikov, V. P., Wallace, J. M., & Bladé, I. (1999). The effective number of spatial degrees of freedom of a time-varying field. *Journal of Climate*, *12*, 1990–2009. https://doi.org/10.1175/1520-0442(1999)012<1990:TENOSD>2.0.CO;2

CMEMS Product User Manual (2018). CMEMS product user manual for sea level SLA products version 4.0, Copernicus Marine Environment Monitoring Service. http://marine.copernicus.eu/documents/PUM/CMEMS-SL-PUM-008-032-051.pdf.

Campbell, J. W. (1995). The lognormal distribution as a model for bio-optical variability in the sea. *Journal of Geophysical Research*, *100*, 13,237–13,254. https://doi.org/10.1029/95JC00458

Chavanne, C., Flament, P., Lumpkin, R., Dousset, B., & Bentamy, A. (2002). Scatterometer observations of wind variations induced by oceanic islands: Implications for wind-driven ocean circulation. *Canadian Journal of Remote Sensing*, *28*, 466–474. https://doi.org/10.5589/m02-047

Chelton, D. B., Bernal, P. A., & McGowan, J. A. (1982). Large-scale interannual physical and biological interaction in the California Current. *Journal of Marine Research*, *40*, 1095–1125.

Chelton, D. B., & Davis, R. E. (1982). Monthly mean sea-level variability along the west coast of North America. *Journal of Physical Oceanography*, *12*, 757–784.

Chelton, D. B., & Freilich, M. H. (2005). Scatterometer-based assessment of 10-m wind analyses from the observational ECMWF and NCEP numerical weather prediction models. *Monthly Weather Review*, *133*, 409–429.

Chereskin, T. K., & Niiler, P. P. (1994). Circulation in the Ensenada Front—September 1988. *Deep Sea Research*, *41*, 1251–1287.

Clemensha, R. E. S., Gershunov, A., Iacobellis, S. F., Williams, A. P., & Cayan, D. R. (2016). The northward march of summer low cloudiness along the California coast. *Geophysical Research Letters*, *43*, 1287–1295. https://doi.org/10.1002/2015GL067081

Dee, D. P., Uppala, S. M., Simmons, A. J., Berrisford, P., Poli, P., Kobayashi, S., et al. (2011). The ERA-interim reanalysis: Configuration and performance of the data assimilation system. *Quarterly Journal of the Royal Meteorological Society*, *137*, 553–597. https://doi.org/10.1002/qj.828

Di Lorenzo, E. (2003). Seasonal dynamics of the surface circulation in the Southern California Current System. *Deep Sea Research*, *50*, 2371–2388.

Di Lorenzo, E., Schneider, N., Cobb, K. M., Franks, P. J. S., Chhak, K., Miller, A. J., et al. (2008). North Pacific Gyre Oscillation links ocean climate and ecosystem change. *Geophysical Research Letters*, *35*, L08607. https://doi.org/10.1029/2007GL032838

Dong, C., Idica, E. Y., & McWilliams, J. C. (2009). Circulation and multiple-scale variability in the Southern California Bight. *Progress in Oceanography*, *82*, 168–190. https://doi.org/10.1016/j.pocean.2009.07.005

Dong, C., Lin, X., Liu, Y., Nencioli, F., Chao, Y., Guan, Y., et al. (2012). Three-dimensional oceanic eddy analysis in the Southern California Bight from a numerical product. *Journal of Geophysical Research*, *117*, C00H14. https://doi.org/10.1029/2011JC007354

Dottori, M., & Clarke, A. J. (2009). Rossby waves and the interannual and interdecadal variability of temperature and salinity off California. *Journal of Physical Oceanography*, *39*, 2543–2561.

Ebisuzaki, W. (1997). A method to estimate the statistical significance of a correlation when the data are serially correlated. *Journal of Climate*, *10*, 2147–2153. https://doi.org/10.1175/1520-0442(1997)010<2147:AMTETS>2.0.CO;2

Enfield, D. B., & Allen, J. S. (1980). On the structure and dynamics of monthly mean sea level anomalies along the Pacific coast of North and South America. *Journal of Physical Oceanography*, *10*, 557–578.

Fewings, M. R. (2017). Large-scale structure in wind forcing over the California Current System in summer. *Monthly Weather Review*, *145*, 4227–4247. https://doi.org/10.1175/MWR-D-17-0106.1

Fewings, M. R., Washburn, L., Dorman, C. E., Gotschalk, C., & Lombardo, K. (2016). Synoptic forcing of wind relaxations at Pt.Conception, California. *Journal of Geophysical Research: Oceans*, *121*, 5711–5730. https://doi.org/10.1002/2016JC011699

Fiedler, P. C., & Mantua, N. J. (2017). How are warm and cool years in the California current related to ENSO? *Journal of Geophysical Research: Oceans*, *122*, 5936–5951. https://doi.org/10.1002/2017JC013094

Fore, A. G., Stiles, B. W., Chau, A. H., Williams, B. A., Dunbar, R. S., & Rodríguez, E. (2014). Point-wise wind retrieval and ambiguity removal improvements for the QuikSCAT climatological data set. *IEEE Transactions on Geoscience and Remote Sensing*, *52*(1), 51–59. https://doi.org/10.1109/TGRS.2012.2235843

Freeland, H. J., Gatien, G., Huyer, A., & Smith, R. L. (2003). Cold halocline in the Northern California Current: An invasion of subarctic water. *Geophysical Research Letters*, *30*(3), 1141. https://doi.org/10.1029/2002GL016663

Frischknecht, M., Munnich, M., & Gruber, N. (2017). Local atmospheric forcing driving an unexpected California Current System response during the 2015–2016 El Niño. *Geophysical Research Letters*, *44*, 304–311. https://doi.org/10.1002/2016GL071316

Gaube, P., Chelton, D. B., Strutton, P. G., & Behrenfeld, M. J. (2013). Satellite observations of chlorophyll, phytoplankton biomass, and Ekman pumping in nonlinear mesoscale eddies. *Journal of Geophysical Research: Oceans*, *118*, 6349–6370. https://doi.org/10.1002/2013JC009027

Hickey, B. M. (1992). Circulation over the Santa Monica-San Pedro basin and shelf. *Progress in Oceanography*, *30*, 37–115.

Hickey, B. M. (1998). Coastal oceanography of western North America from the tip of Baja California to Vancouver Island. In A. R. Robinson & K. H. Brink (Eds.), *The sea* (Vol. 11, pp. 345–393). New York: John Wiley.

Hu, C., Lee, Z., & Franz, B. (2012). Chlorophyll a algorithms for oligotrophic oceans: A novel approach based on three-band reflectance difference. *Journal of Geophysical Research*, *117*, C01011. https://doi.org/10.1029/2011JC007395

Jacox, M. G., Fiechter, J., Moore, A. M., & Edwards, C. A. (2015). ENSO and the California Current coastal upwelling response. *Journal of Geophysical Research: Oceans*, *120*, 1691–1702. https://doi.org/10.1002/2014JC010650

Jacox, M. G., Hazen, E. L., Zaba, K. D., Rudnick, D. L., Edwards, C. A., Moore, A. M., & Bograd, S. J. (2016). Impacts of the 2015–2016 El Niño on the California Current System: Early assessment and comparison to past events. *Geophysical Research Letters*, *43*, 7072–7080. https://doi.org/10.1002/2016GL069716

Johnston, T. M. S., & Rudnick, D. L. (2015). Trapped diurnal internal tides, propagating semidiurnal internal tides, and mixing estimates in the California Current System from sustained glider observations, 2006–2012. *Deep-Sea Research Part II*, *112*, 61–78. https://doi.org/10.1016/j.dsr2.2014.03.009

Kahru, M., & Mitchell, B. G. (2000). Influence of the 1997-98 El Niño on the surface chlorophyll in the California Current. *Geophysical Research Letters*, *27*, 2937–2940. https://doi.org/10.1029/2000GL011486

Kahru, M., & Mitchell, B. G. (2001). Seasonal and nonseasonal variability of satellite-derived chlorophyll and colored dissolved organic matter concentration in the California Current. *Journal of Geophysical Research*, *106*, 2517–2529. https://doi.org/10.1029/1999JC000094

Kilpatrick, T., Schneider, N., & Di Lorenzo, E. (2011). Generation of low-frequency spiciness variability in the thermocline. *Journal of Physical Oceanography*, *41*, 365–377. https://doi.org/10.1175/2010JPO4443.1

Kilpatrick, T., & Xie, S.-P. (2016). Circumventing rain-related errors in scatterometer wind observations. *Journal of Geophysical Research: Oceans*, *121*, 9422–9440. https://doi.org/10.1002/2016JD025105

Kim, S. Y., & Cornuelle, B. D. (2015). Coastal ocean climatology of temperature and salinity off the Southern California Bight: Seasonal variability, climate index correlation, and linear trend. *Progress in Oceanography*, *138*, 136–157. https://doi.org/10.1016/j.pocean.2015.08.001

King, A. L., & Barbeau, K. A. (2007). Evidence for phytoplankton iron limitation in the southern California Current System. *Marine Ecology Progress Series*, *342*, 91–103. https://doi.org/10.3354/meps342091

King, A. L., & Barbeau, K. A. (2011). Dissolved iron and macronutrient distributions in the southern California Current System. *Journal of Geophysical Research*, *116*, C03018. https://doi.org/10.1029/2010JC006324

Koracin, D., Dorman, C. E., & Dever, E. P. (2004). Coastal perturbations of marine-layer winds, wind stress, and wind stress curl along California and Baja California in June 1999. *Journal of Physical Oceanography*, *34*, 1152–1173.

Landry, M. R., Ohman, M. D., Goericke, R., Stukel, M. R., Barbeau, K. A., Bundy, R., & Kahru, M. (2012). Pelagic community responses to a deep-water front in the California Current Ecosystem: Overview of the A-Front study. *Journal of Plankton Research*, *34*, 739–748. https://doi.org/10.1093/plankt/fbs025

Large, W. G., & Pond, S. (1982). Sensible and latent heat flux measurements over the ocean. *Journal of Physical Oceanography*, *12*, 464–482.

Legaard, K. R., & Thomas, A. C. (2006). Spatial patterns in seasonal and interannual variability of chlorophyll and sea surface temperature in the California Current. *Journal of Geophysical Research*, *111*, C06032. https://doi.org/10.1029/2005JC003282

Lynn, R. J., & Simpson, J. J. (1987). The California Current system: The seasonal variability of its physical characteristics. *Journal of Geophysical Research*, *92*, 12,947–12,966. https://doi.org/10.1029/JC092iC12p12947

Mantua, N. J., Hare, S. R., Zhang, Y., Wallace, J. M., & Francis, R. C. (1997). A Pacific interdecadal climate oscillation with impacts on salmon production. *Bulletin of the American Meteorological Society*, *78*, 1069–1079.

Marchesiello, P., McWilliams, J. C., & Shchepetkin, A. (2003). Equilibrium structure and dynamics of the California Current System. *Journal of Physical Oceanography*, *33*, 753–783.

McClain, C. R. (2009). A decade of satellite ocean color observations. *Annual Review of Marine Science*, *1*, 19–42. https://doi.org/10.1146/annurev.marine.010908.163650

McCreary, J. P., Kundu, P. K., & Chao, S.-Y. (1987). On the dynamics of the California Current system. *Journal of Marine Research*, *45*, 1–32. https://doi.org/10.1357/002224087788400945

Mulet, S., Rio, M. H., Greiner, E., Picot, N., & Pascual, A. (2013). New global mean dynamic topography from a GOCE geoid model, altimeter measurements and oceanographic in-situ data. In *OSTST Meeting 2013* (pp. 27.) Edinburgh, UK. http://www.aviso.altimetry.fr/fileadmin/documents/OSTST/2013/oral/mulet_MDT_CNES_CLS13.pdf.

NASA Goddard Space Flight Center, O. B. P. G. (2014). Moderate-resolution Imaging Spectroradiometer (MODIS) Aqua Ocean Color Data; 2014 reprocessing. https://doi.org/10.5067/AQUA/MODIS_OC.2014.0 NASA OB.DAAC, Greenbelt, MD, USA. Dataset accessed 2018-03-19.

NASA Goddard Space Flight Center, O. B. P. G. (2018a). Moderate-resolution Imaging Spectroradiometer (MODIS) Aqua Chlorophyll Data; 2018 reprocessing. https://doi.org/10.5067/AQUA/MODIS/L3M/CHL/2018 NASA OB.DAAC, Greenbelt, MD, USA. Dataset accessed 2018-01-22.

NASA Goddard Space Flight Center, O. B. P. G. (2018b). Sea-viewing Wide Field-of-view Sensor (SeaWiFS) chlorophyll data; 2018 reprocessing. https://doi.org/10.5067/ORBVIEW-2/SEAWIFS/L3M/CHL/2018 NASA OB.DAAC, Greenbelt, MD, USA. Dataset accessed 2018-03-28.

O'Neill, L., Haack, T., & Durland, T. (2015). Estimation of time-averaged surface divergence and vorticity from satellite ocean vector winds. *Journal of Climate*, *28*, 7596–7620. https://doi.org/10.1175/JCLI-D-15-0119.1

Pelaez, J., & McGowan, J. A. (1986). Phytoplankton pigment patterns in the California Current as determined by satellite. *Limnology and Oceanography*, *31*, 927–950.

Reynolds, R. W., Smith, T. M., Liu, C., Chelton, D. B., Casey, K. S., & Schlax, M. G. (2007). Daily high-resolution-blended analyses for sea surface temperature. *Journal of Climate*, *20*, 5473–5496. https://doi.org/10.1175/2007JCLI1824.1

Risien, C. M., & Chelton, D. B. (2008). A global climatology of surface wind and wind stress fields from eight years of quikSCAT scatterometer data. *Journal of Physical Oceanography*, *38*, 2379–2413. https://doi.org/10.1175/2008JPO3881.1

Rudnick, D. L., Zaba, K. D., Todd, R. E., & Davis, R. E. (2017). A climatology of the California Current System from a network of underwater gliders. *Progress in Oceanography*, *154*, 64–106. https://doi.org/10.1016/j.pocean.2017.03.002

Rykaczewski, R. R., & Checkley, D. M. (2008). Influence of ocean winds on the pelagic ecosystem in upwelling regions. *Proceedings of the National Academy of Sciences of the United States of America*, *105*, 1965–1970. https://doi.org/10.1073/pnas.0711777105

Schneider, N., & Cornuelle, B. D. (2005). The forcing of the Pacific decadal oscillation. *Journal of Climate*, *18*, 4355–4373.

Schneider, N., Di Lorenzo, E., & Niiler, P. P. (2005). Salinity variations in the Southern California Current. *Journal of Physical Oceanography*, *35*, 1421–1436.

Schwing, F. B., Murphree, T., deWitt, L., & Green, P. M. (2002). The evolution of oceanic and atmospheric anomalies in the northeast Pacific during the El Niño and La Niña events of 1995–2001. *Progress in Oceanography*, *54*, 459–491. https://doi.org/10.1016/S0079-6611(02)00064-2

SeaPAC (2013). QuikSCAT level 2B ocean wind vectors in 12.5 km slice composites version 3. https://doi.org/10.5067/QSX12-L2B01, ver.3. PO.DAAC, CA, USA. Dataset accessed 2014-11-06.

Seo, H., Brink, K. H., Dorman, C. E., Koracin, D., & Edwards, C. A. (2012). What determines the spatial pattern in summer upwelling trends on the U.S. West Coast? *Journal of Geophysical Research*, *117*, C08012. https://doi.org/10.1029/2012JC008016

Strub, P. T., James, C., Thomas, A. C., & Abbott, M. R. (1990). Seasonal and nonseasonal variability of satellite-derived surface pigment concentration in the California Current. *Journal of Geophysical Research*, *95*, 11,501–11,530. https://doi.org/10.1029/JC095iC07p11501

Thomas, A. C., Brickley, P., & Weatherbee, R. (2009). Interannual variability in chlorophyll concentrations in the Humboldt and California Current Systems. *Progress in Oceanography*, *83*, 386–392. https://doi.org/10.1016/j.pocean.2009.07.020

Thomas, A. C., Huang, F., Strub, P. T., & James, C. (1994). Comparison of the seasonal and interannual variability of phytoplankton pigment concentrations in the Peru and California Current Systems. *Journal of Geophysical Research*, *99*, 7355–7370. https://doi.org/10.1029/93JC02146

Thomas, A. C., & Strub, P. T. (1990). Seasonal and interannual variability of pigment concentrations across a California current frontal zone. *Journal of Geophysical Research*, *95*, 13,023–13,042.

Thomas, A. C., Strub, P. T., Weatherbee, R. A., & James, C. (2012). Satellite views of Pacific chlorophyll variability: Comparisons to physical variability, local versus nonlocal influences and links to climate indices. *Deep-Sea Research Part II*, *77-80*, 99–106. https://doi.org/10.1016/j.dsr2.2012.04.008

Todd, R. E., Rudnick, D. L., Mazloff, M. R., Davis, R. E., & Cornuelle, B. D. (2011). Poleward flows in the southern California Current System: Glider observations and numerical simulation. *Journal of Geophysical Research*, *116*, C02026. https://doi.org/10.1029/2010JC006536

Venegas, R. M., Strub, P. T., Beier, E., Letelier, R., Thomas, A. C., Cowles, T., et al. (2008). Satellite-derived variability in chlorophyll, wind stress, sea surface height, and temperature in the northern California Current System. *Journal of Geophysical Research*, *113*, C03015. https://doi.org/10.1029/2007JC004481

Venrick, E. L. (2012). Phytoplankton in the California current system off southern California: Changes in a changing environment. *Progress in Oceanography*, *104*, 46–58. https://doi.org/10.1016/j.pocean.2012.05.005

Xie, S.-P., Liu, W. T., Liu, Q., & Nonaka, M. (2001). Far-reaching effects of the Hawaiian Islands on the Pacific Ocean-atmosphere system. *Science*, *292*, 2057–2060. https://doi.org/10.1126/science.1059781

Yoder, J. A., & Kennelly, M. A. (2006). What have we learned about ocean variability from satellite ocean color images? *Oceanography*, *19*, 152–171.